ROYAL SOCIETY OPEN SCIENCE

royalsocietypublishing.org/journal/rsos

Research

Cite this article: Bai H *et al*. 2020 High-efficient fabrication of core-shell-shell structured SiO_2@$GdPO_4$:Tb@SiO_2 nanoparticles with improved luminescence. *R. Soc. Open Sci.* **7**: 192235.
http://dx.doi.org/10.1098/rsos.192235

Received: 5 January 2020
Accepted: 23 April 2020

Subject Category:
Chemistry

Subject Areas:
materials science/inorganic chemistry/nanotechnology

Keywords:
SiO_2, core-shell-shell structure, rare earth phosphate, luminescence, nanoparticles

Author for correspondence:
Jinrong Bao
e-mail: jinrongbao@imu.edu.cn

†Present address: School of Chemistry and Chemical Engineering, Inner Mongolia University, Hohhot 010021, China.

This article has been edited by the Royal Society of Chemistry, including the commissioning, peer review process and editorial aspects up to the point of acceptance.

Electronic supplementary material is available online at https://doi.org/10.6084/m9.figshare.c.4992599.

ROYAL SOCIETY OF CHEMISTRY

THE ROYAL SOCIETY PUBLISHING

High-efficient fabrication of core-shell-shell structured SiO_2@$GdPO_4$:Tb@SiO_2 nanoparticles with improved luminescence

He Bai[1], Yunjiang Yang[1], Jinrong Bao[1,†], Anping Wu[1], Yan Qiao[1], Xueyuan Guo[1], Mingyuan Wang[1], Wenxian Li[1], Ying Liu[1] and Xiaowei Zhu[2]

[1]Inner Mongolia Key Laboratory of Chemistry and Physics of Rare Earth Materials, College of Chemistry and Chemical Engineering, and [2]College of Pharmacology, Inner Mongolia Medical University, Hohhot 010110, People's Republic of China

JB, 0000-0002-2480-7330; WL, 0000-0002-0938-6910

SiO_2@$GdPO_4$:Tb@SiO_2 nanoparticles with core-shell-shell structure were successfully synthesized by a cheap silane coupling agent grafting method at room temperature. This method not only homogeneously coated rare-earth phosphate nanoparticles on the surface of silica spheres but also saved the use of rare-earth resources. The obtained nanoparticles consisted of SiO_2 core with a diameter of approximately 210 nm, $GdPO_4$:Tb intermediate shell with thickness of approximately 7 nm, and SiO_2 outer shell with thickness of approximately 20 nm. This unique core-shell-shell structured nanoparticles exhibited strong luminescence properties compared with $GdPO_4$:Tb nanoparticles. The core-shell-shell structured nanoparticles can effectively quench the intrinsic fluorescence of bovine serum albumin through a static quenching mode. The as-synthesized nanoparticles show great potential in biological cell imaging and cancer treatment.

1. Introduction

Because of the unique 4f shell of the ions, lanthanide compounds often show good electronic, optical and magnetic characteristics. The lanthanide compounds have attracted considerable interest with major applications in optics, plasma display, drug delivery, magnets and biological labelling [1–4]. A particularly intriguing use of lanthanide phosphate ($LnPO_4$) is in optoelectronic devices and biological fluorescence labelling, which may be based on its

excellent luminescence, low toxicity, long decay time, and chemical stability [5–7]. Among the rare-earth phosphates, gadolinium phosphate ($GdPO_4$) is an important host matrix for luminescent lanthanide ion-doped nanophosphors [8]. $GdPO_4$ matrix nanoparticles have been proved to be a potential multi-functional nano-platform for magnetic resonance imaging (MR) and effective optical imaging materials [9]. In recent years, gadolinium phosphate nanoparticles have been synthesized by various methods. For example, Rodriguez-Liviano *et al*. have prepared $GdPO_4:Eu^{3+}$ nanoparticles via microwave-assisted heating method, which showed potential applications in biolabels [10]. $GdPO_4:Eu^{3+}$ nanoparticles also have been synthesized by co-precipitation, and the nanoparticles can emit intense orange-red fluorescence [11]. $GdPO_4:Eu^{3+}/Tb^{3+}$ was synthesized via typical hydrothermal method; the nanoparticles can obtain a bright colour-tunable photoluminescence from red, orange, yellow to green region when the $GdPO_4$ nanoparticles are co-doped with Eu^{3+} and Tb^{3+} ions [12]. However, most conventional synthesis methods required high temperature, pressure and expensive precursors.

In particular, the lanthanide compounds nano phosphors have poor aqueous solubility and dispersion, and then their biocompatible and biological applications might be limited [13]. In order to enhance the solubility and dispersion in aqueous solution of some namomaterials, the surface of the nanomaterials were modified by polyethylene glycol derivative, poly (acrylic acid) and silica. For example, PEG-$NaYF_4$: Yb/Tm was synthesized by a layer-by-layer strategy, which has great potential in bio-imaging and photodynamic therapy [14]. Hexagonal phase $NaYF_4$:Yb,Er@PAA can be synthesized by the modification method, which has great potential in bio-probes [15]. Xu *et al.* prepared self-assembled Ni/Co phosphide composite N-doped carbon spheres via a hydrothermal process, which had abundant exposed active sites for the hydrogen evolution reaction [16]. The obtained Artemia cyst shell (ACS)–TiO_2–MoS_2 ternary porous structure has a good reduction effect on 4-NP and 2-NA, which is obviously higher than the reduction effect of ACS–TiO_2 and MoS_2 under the same conditions [17]. Therefore, the synthesis of SiO_2-lanthanide phosphate/oxide nanomaterials with core-shell structure has attracted considerable attention due to the decrease in use of rare earth and its non-toxicity. Core-shell structured $SiO_2@Y_2O_3:Eu^{3+}$ nanopowder was found to be appropriate as a fluorescent marker for latent fingerprint recognition, security ink and solid-state lighting applications [18]. Xu *et al*. have synthesized a luminescent and mesoporous core-shell structured $Gd_2O_3:Eu^{3+}@SiO_2$ nanocomposite and make it as a drug carrier [19]. In our previous studies, we have synthesized $SiO_2@EuPO_4$ by co-precipitation using triethyl phosphate [20]. It was found that the core-shell nanostructure can significantly improve the emission strength of the material. However, because the hydrolysis rate of tributyl phosphate was not easy to control, the coating uniformity was poor. By bridging ligand organosilane $HOOCC_6H_4N(CONH(CH_2)_3Si(OCH_2CH_3)_3)_2$ (MABA-Si) connected with SiO_2 submicrospheres and rare earth ion, it makes $CePO_4$:Tb nanoparticles coated uniformly on the surface of SiO_2 submicrospheres. We also synthesized core-shell-shell structured $SiO_2@CePO_4:Tb@SiO_2$ [21]. In addition, silica shell can greatly improve the stability of $SiO_2@GdPO_4$: $Tb@SiO_2$ nanoparticles through protecting the core materials from dissolution or hydrolysis. However, the $-Si(OCH_2CH_3)_3$ group of MABA-Si ligand was easy to hydrolyse in the air, so it is difficult to connect with SiO_2 submicrospheres. When SiO_2 was used as core and shell of the core-shell-shell particles, it might not only decrease the consumption of rare earth but also give more functions to nanomaterials [21–23].

In this paper, we report a room-temperature silane coupling agent grafting method to simultaneously graft 3-(aminopropyl) triethoxysilane (APTES) on the surface of the silicon spheres and bond with carboxyl of maleic anhydride (MAH). By means of this way, the reaction of silane coupling agent APTES connected with SiO_2 spheres and rare-earth phosphate is easy to carry out. Furthermore, nano rare-earth phosphate can be homogeneously coated on the surface of silica spheres. The obtained $SiO_2@GdPO_4:Tb@SiO_2$ nanoparticles show a core-shell-shell structure with uniform size and coating layer. The SiO_2 can be functioned as fixed centre core and protected layer shell, respectively. These unique structures endow $SiO_2@GdPO_4:Tb@SiO_2$ nanoparticles good luminescence properties. Moreover, the interaction between the core-shell-shell structured nanoparticles and BSA in the simulated physiological conditions was studied. The core-shell-shell structured $SiO_2@GdPO_4:Tb@SiO_2$ nanoparticles makes nanoparticles highly biocompatible and non-toxic, which would expand their potential applications in the field of biomedicine.

2. Material and methods

2.1. Material and reagents

All chemicals were analytical, unpurified and used as received. Ammonia, Tb_4O_7 (99.99%), $Gd(NO_3)_3{\cdot}6H_2O$, $(NH_4)_2HPO_4$ and cetyltrimethyl ammonium bromide (CTAB) were all purchased by

Shanghai McLean Biochemical Technology Corporation Limited. 3-(aminopropyl) triethoxysilane (APTES), MAH and tetraethoxysilane (TEOS) were achieved from Aladdin (Shanghai, China). Bovine serum albumin (BSA, biochemical reagent, average molecular weight of 66 000 g mol^{-1}) was supplied by Beijing bailingwei Technology Corporation Limited (Beijing, China). The terbium nitrate powder prepared from Tb_4O_7 was dissolved in 10% nitric acid, then evaporated and dried in vacuum.

2.2. Synthesis of SiO_2@$GdPO_4$:Tb@SiO_2 nanoparticles

The core-shell structured SiO_2@$GdPO_4$:Tb was prepared by the following steps. The SiO_2 spheres were synthesized by the Stöber method [24], in which 0.2 g were dispersed in anhydrous ethanol via ultrasonication. Then 0.5 ml APTES was put into above ethanol suspension under stirring for 12 h. After centrifugation, the above as-prepared product (labelled as SiO_2@NH_2) was dispersed in ethanol, and dropped in 1.5 mmol MAH ethanol solution stirring for 6.0 h. The obtained solution (labelled as SiO_2@MAH-Si) was centrifuged. Then, it was dispersed in 10 ml anhydrous ethanol followed by adding of 0.098 mol l^{-1} $Ln(NO_3)_3$ (Gd^{3+} 95%, Tb^{3+} 5%) ethanol solution, which was further stirred for 4 h. Finally, 0.0216 g $(NH_4)_2HPO_4$ was added, and continuously reacted for 2 h. The SiO_2@$GdPO_4$:Tb was obtained by further centrifugation and washing with ethanol three times.

For the synthesis of the SiO_2@$GdPO_4$:Tb@SiO_2 nanoparticles, the above as-prepared SiO_2@$GdPO_4$:Tb was dispersed in 20 ml 50% ethanol solution via ultrasonication. Then, 0.15 g of cetyltrimethyl ammonium bromide and 0.3 ml of tetraethoxysilane (TEOS) was added to above suspension under stirring for 6 h. After centrifugation, the obtained white solid were further washed with ethanol three times. The white solid was dried at 80°C for 6 h, which was then treated at 600°C for 2 h under nitrogen atmosphere.

2.3. Interaction between BSA and SiO_2@$GdPO_4$:Tb@SiO_2 nanoparticles

The whole BSA binding experiment was performed in Tris–HCl buffer solution with pH = 7.4. The solutions of BSA and the core-shell-shell structured SiO_2@$GdPO_4$:Tb@SiO_2 nanoparticles were prepared by dissolving them in the Tris–HCl buffer solution to obtain the desired concentrations. In the fluorescence quenching experiment of BSA, the quenching of BSA was achieved by keeping BSA as a fixed concentration and adding core-shell nanoparticles with different concentrations ($a = 0.000$, $b = 1.85 \times 10^{-5}$, $c = 3.70 \times 10^{-5}$, $d = 5.55 \times 10^{-5}$, $e = 7.42 \times 10^{-5}$, $f = 9.25 \times 10^{-5}$, $g = 1.11 \times 10^{-4}$, $h = 1.29 \times 10^{-4}$, $i = 1.48 \times 10^{-4}$ and $j = 1.66 \times 10^{-4}$ mol l^{-1}). Fluorescence measurements were made at 293 K, 303 K and 313 K. The fluorescence spectra of BSA were tested at an excitation wavelength at 280 nm and an emission wavelength at 335 nm after addition of the core-shell-shell nanoparticles.

2.4. Characterization

The morphology of the products was characterized by transmission electron microscopy (TEM; FEI Tecnai F20, USA) and scanning electronic microscopy (SEM; Hitachi S-4800, Japan). The crystal structure is investigated by X-ray powder diffraction (XRD; RIGAKU, Japan) using Cu K_α radiation. Infrared spectrum of the solid powders was determined in the range of 400–4000 cm^{-1} (FT-IR; Bruker, Germany). The luminescence spectra of powders was examined on a fluorescence photometer (FL; Edinburgh S980, UK).

3. Results and discussion

XRD analysis investigated the phase purity and crystal structure of the as-prepared products. Figure 1 shows the XRD patterns of SiO_2 and SiO_2@$GdPO_4$:Tb@SiO_2 nanoparticles. It can be seen that two diffraction peaks at $2\theta = 8°$ and 22° from amorphous SiO_2 were detected on both samples. Several new weak diffraction peaks appeared in SiO_2@$GdPO_4$:Tb@SiO_2, which were matched with monoclinic phase of $GdPO_4$ (JCPDS No. 32–386). The microstructure and size of the as-obtained samples were examined from TEM images as shown in figure 2. TEM image of SiO_2 (figure 2*a*) and the particle size distribution indicated that SiO_2 spheres have a regular morphology and excellent monodispersity with diameters about 210 nm. When SiO_2 were coated with $GdPO_4$:Tb, the surface of the obtained SiO_2@$GdPO_4$:Tb spheres becomes rough and the diameter of SiO_2@$GdPO_4$:Tb is about 225 nm. To make the nanoparticles more functional, the surface of the SiO_2@$GdPO_4$:Tb spheres were modified by

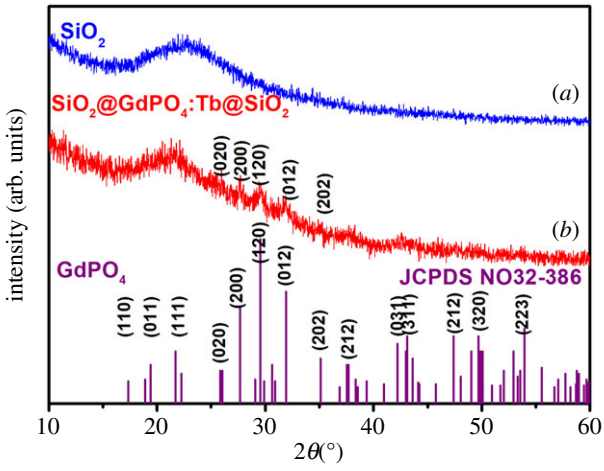

Figure 1. XRD patterns of (*a*) SiO_2, (*b*) SiO_2@$GdPO_4$:Tb@SiO_2.

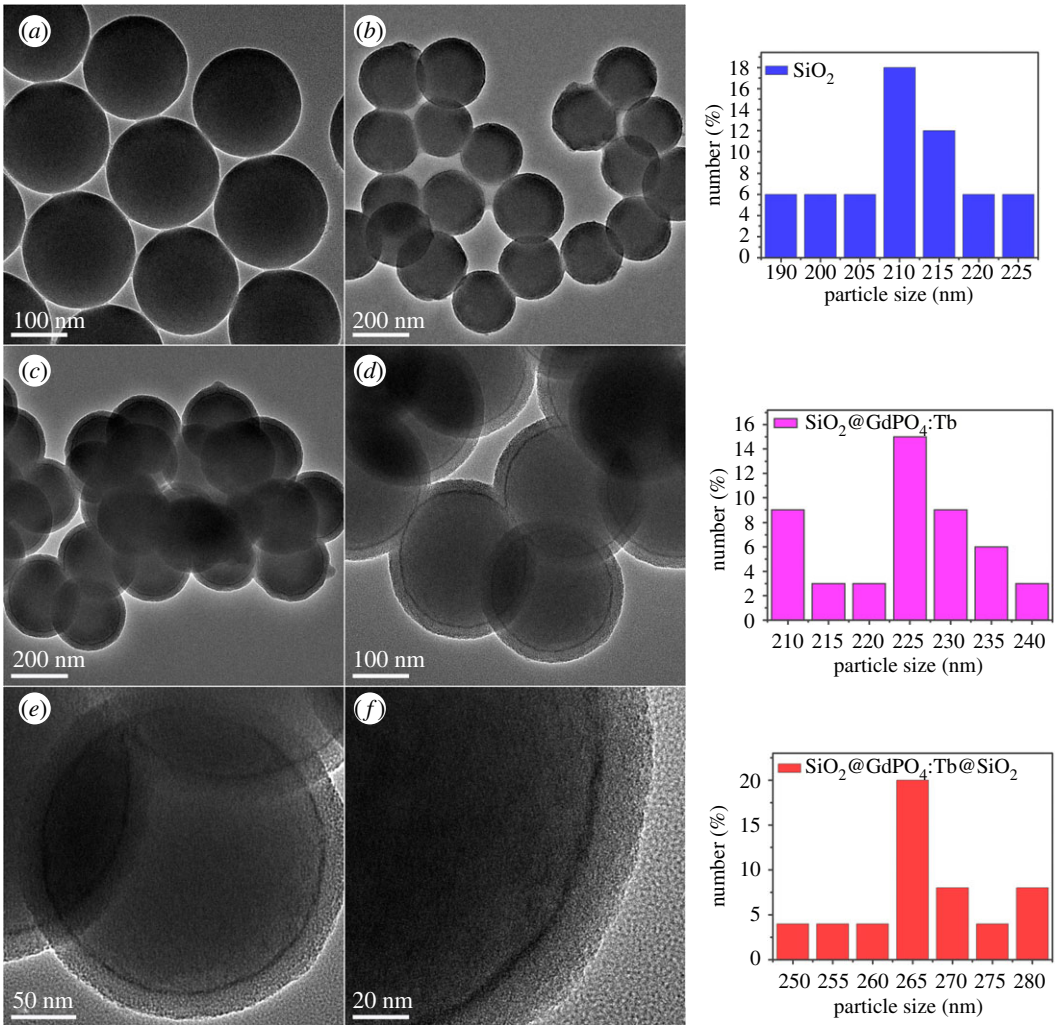

Figure 2. TEM images of the products (*a*) SiO_2, (*b*) SiO_2@$GdPO_4$:Tb, (*c–f*) SiO_2@$GdPO_4$:Tb@SiO_2, and corresponding size distribution images.

SiO_2 as shown in figure 2*c–f* at different magnification. It can be shown that the product SiO_2@$GdPO_4$:Tb@SiO_2 have obvious core-shell-shell structures and smooth surfaces. The corresponding particle size distribution indicated that the core-shell-shell structures have diameters of about 265 nm. The thickness of the intermediate shell $GdPO_4$:Tb was approximately 7 nm, and the diameter of the SiO_2 core and outer shell was approximately 210 and approximately 20 nm, respectively. In addition, we

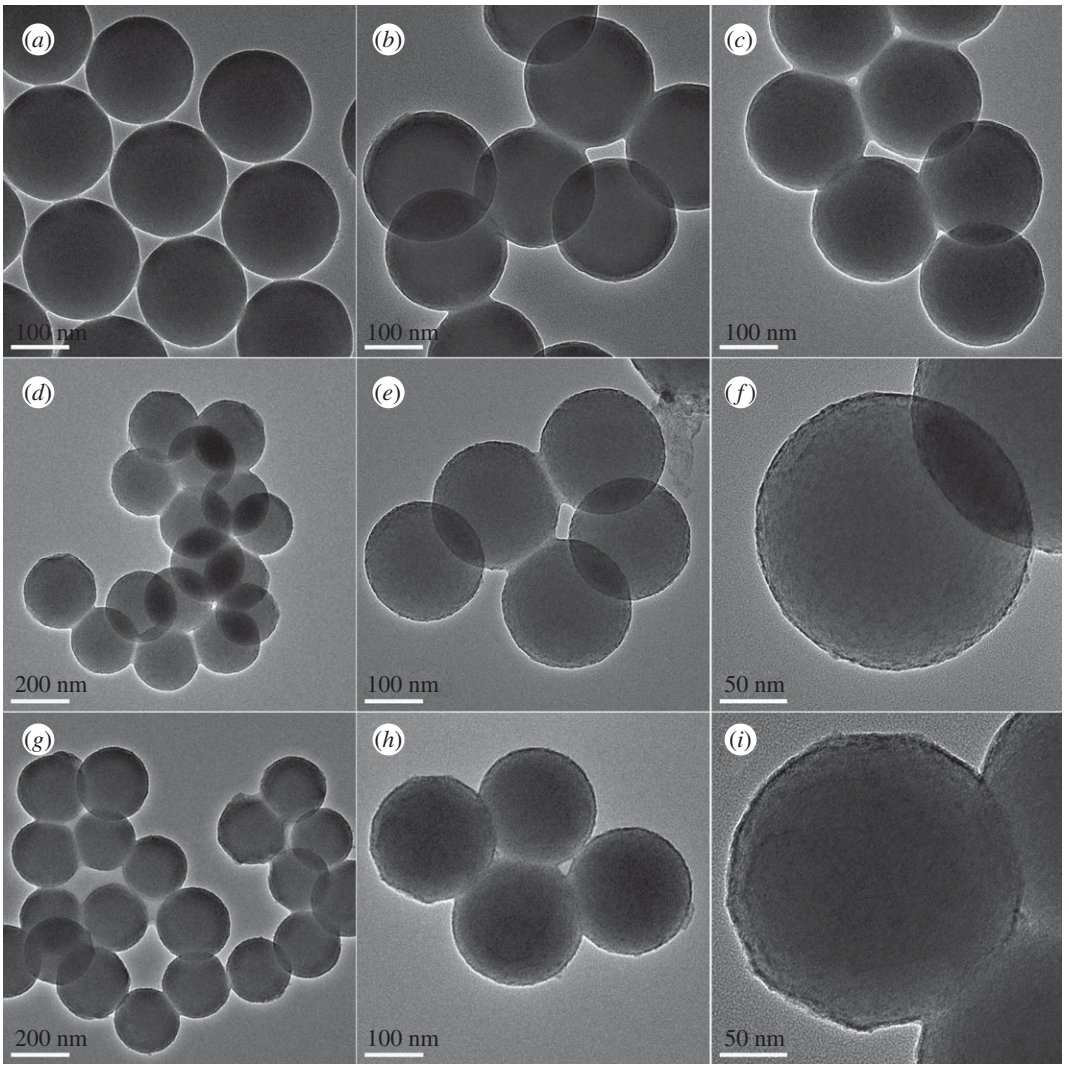

Figure 3. TEM images of the products synthesized in different stages: (*a*) SiO_2, (*b*) SiO_2@NH_2, (*c*) SiO_2@MAH-Si, (*d–f*) SiO_2@MAH-Si-Gd:Tb, (*g–i*) SiO_2@$GdPO_4$:Tb.

can clearly see that intermediate shell $GdPO_4$:Tb was uniformly grown on the surface of the SiO_2 core. The corresponding FESEM images of the as-synthesized products are shown in electronic supplementary material, figure S1. It can be seen that SiO_2 spherical particles with an average size of 210 nm were non-aggregated and uniformly distributed (electronic supplementary material, figure S1a and b). The diameter of SiO_2@$GdPO_4$:Tb increased to 225 nm after $GdPO_4$:Tb coating, and the surface became rougher (electronic supplementary material, figure S1c and d). Furthermore, SiO_2@$GdPO_4$:Tb@SiO_2 still maintained a good spherical shape, while the particle size was increased to 265 nm (electronic supplementary material, figure S1e and f). Electronic supplementary material, figure S1e,f shows SiO_2@$GdPO_4$:Tb@SiO_2 still maintained a good spherical shape with a size of about 265 nm. Meanwhile, SiO_2@$GdPO_4$:Tb@SiO_2 nanoparticles also had a high BET surface area of 62 $m^2\,g^{-1}$ (electronic supplementary material, figure S2).

We further characterized the products at various synthesis stages by TEM and IR. Firstly, figure 3*a* demonstrates that the surface of SiO_2 spheres obtained from the hydrolysis of TEOS was very smooth, and the diameter of SiO_2 sphere was about 210 nm. In the corresponding IR spectra, the vibration of Si-OH of SiO_2 was found at 952 cm^{-1} (electronic supplementary material, figure S3a), which would provide active bonds for grafting. Secondly, after APTES was grafted on the surface of SiO_2 spheres through Si-O-Si bond that of $-NH_2$ group appeared at 1640 cm^{-1} (electronic supplementary material, figure S3b), figure 3*b* demonstrates that the diameters of the SiO_2@NH_2 nanoparticles further increased approximately 2 nm. Thirdly, the SiO_2@MAH-Si nanoparticles were obtained by APTES bonded with MAH. Figure 3*c* demonstrates that there was no obvious change in thickness after

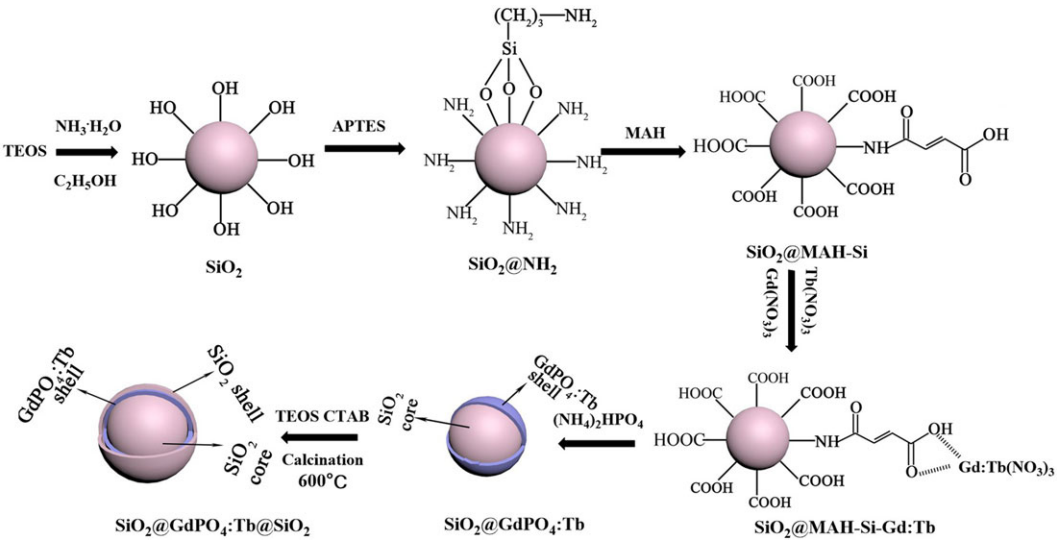

Figure 4. Schematic illustration showing the formation mechanism of core-shell-shell structured SiO_2@$GdPO_4$:Tb@SiO_2.

APTES bonded with MAH. However, three new stretching vibration peaks including −COOH group at 1728 cm^{-1} and −CONH- group at 1632 and 1596 cm^{-1} appeared, which suggested that there was a bond connection between MAH and APTES (electronic supplementary material, figure S3c). TEM images of figure 3*d–f* show that plenty of small particles grown on the surface of SiO_2@MAH-Si nanoparticles after rare-earth ions were coordinated with −COOH of MAH. Simultaneously, the stretching vibration peak of −COOH group was shifted to 1720 cm^{-1} (electronic supplementary material, figure S3d). In the next step, the $GdPO_4$:Tb nanoparticles were formed on the surface of SiO_2 spheres by the substitution reaction of PO_4^{3-}. TEM images of figure 3*g–i* show that the surface of SiO_2@$GdPO_4$:Tb nanoparticles became rough and the rough layer thickness was approximately 7 nm. Therefore, it is reasonable to conclude that $GdPO_4$:Tb layer with thickness of approximately 7 nm have been uniformly coated on the SiO_2 core through substitution reaction. Finally, SiO_2 outer shell was covered on the surface of SiO_2@$GdPO_4$:Tb nanoparticles in the presence of CTAB,through the hydrolysis process of TEOS. CTAB formed a molecular layer on the surface of the silicon core in the reaction system, which would guarantee uniform hydrolysis and growth for TEOS. After calcination, the core-shell-shell structured SiO_2@$GdPO_4$:Tb@SiO_2 nanoparticles were obtained (figures 1 and 2). Energy-dispersive X-ray spectroscopy (EDX) of core-shell-shell structured SiO_2@$GdPO_4$:Tb@SiO_2 was conducted (electronic supplementary material, figure S4); it can be clearly seen that the weight percentages of Si, P, Gd and Tb are 36.73%, 0.74%, 5.79% and 0.29%, respectively. The schematic of core-shell-shell structured SiO_2@$GdPO_4$:Tb@SiO_2 formation process is illustrated in figure 4. Furthermore, functionalized SiO_2@$GdPO_4$:Tb@SiO_2 nanoparticles can be reused after calcination. In other words, the adsorbed proteins and biomolecules can be removed from the surface of nanoparticles after heat treatment of the functionalized SiO_2@$GdPO_4$:Tb@SiO_2 nanoparticles.

The luminescence property of the core-shell-shell structured SiO_2@$GdPO_4$:Tb@SiO_2 and $GdPO_4$:Tb nanoparticles with prepared hydrothermal method was investigated at room temperature. Excitation spectra showed that the strongest excitation peak of $GdPO_4$:Tb nanoparticles appeared at 273 nm, while the core-shell-shell structured SiO_2@$GdPO_4$:Tb@SiO_2 also appeared at 273 nm (figure 5*a*). When these products were excited at strongest excitation wavelength, the emission peaks centred at 488, 543, 584 and 620 nm, which corresponded to the $^5D_4 \rightarrow {}^7F_6$, $^5D_4 \rightarrow {}^7F_5$, $^5D_4 \rightarrow {}^7F_4$ and $^5D_4 \rightarrow {}^7F_3$ transitions for the Tb^{3+} ion [25], respectively (figure 5*b*). The emission intensity of SiO_2@$GdPO_4$:Tb@SiO_2 was stronger than that of $GdPO_4$:Tb nanoparticles, which is consistent with the measurement results of the quantum yield. The absolute quantum yields of SiO_2@$GdPO_4$:Tb@SiO_2 and $GdPO_4$:Tb were 28.28% and 2.73%, respectively. Meanwhile, the photoluminescence lifetime of the products was also measured. The photoluminescence lifetimes were calculated through the double exponential mode $(\tau) = (A_1\tau_1^2 + A_2\tau_2^2)/(A_1\tau_1 + A_2\tau_2)$ and $I(t) = I_0 + A_1\exp(-t_1/\tau_1) + A_2\exp(-t_2/\tau_2)$. Where $I(t)$ is the photoluminescence intensity, τ_1 and τ_2 stand for the slow and fast terms of the luminescent lifetime, respectively. A_1 and A_2 are the corresponding pre-exponential factors. The average lifetime (τ) of the SiO_2@$GdPO_4$:Tb@SiO_2 and $GdPO_4$:Tb calculated from their fluorescence decay curves shown in electronic supplementary material, figure S5 were 1.38 and 2.18 ms, respectively. The rare-earth

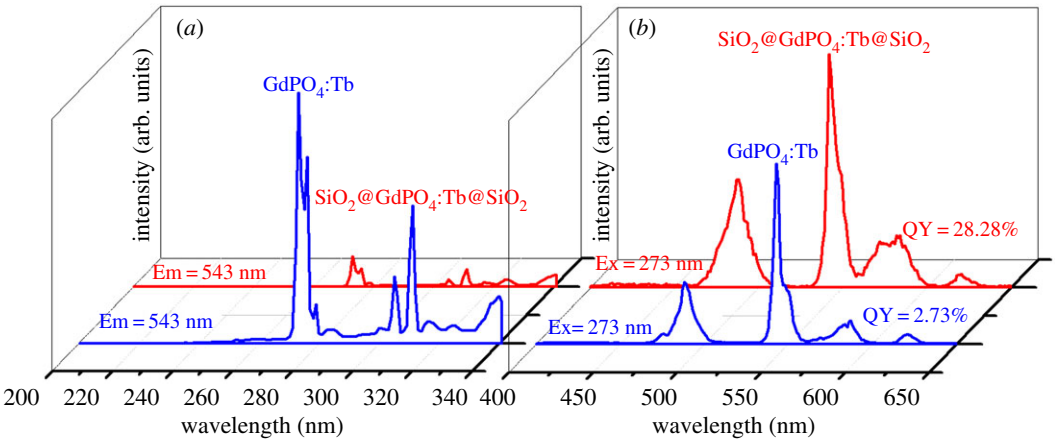

Figure 5. Excitation spectra (*a*) and emission spectra (*b*) of blue line ($GdPO_4$:Tb) and red line (SiO_2@$GdPO_4$:Tb@SiO_2).

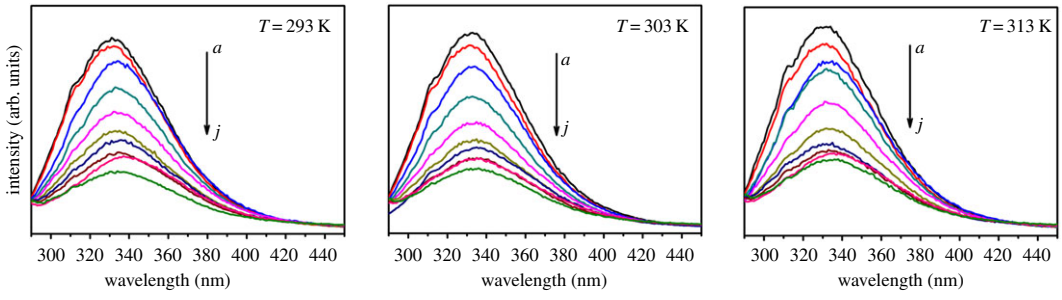

Figure 6. Fluorescence quenching spectra of BSA with various concentrations ($a = 0.000$, $b = 1.85 \times 10^{-5}$, $c = 3.70 \times 10^{-5}$, $d = 5.55 \times 10^{-5}$, $e = 7.42 \times 10^{-5}$, $f = 9.25 \times 10^{-5}$, $g = 1.11 \times 10^{-4}$, $h = 1.29 \times 10^{-4}$, $i = 1.48 \times 10^{-4}$, and $j = 1.66 \times 10^{-4}$ mol l^{-1}) of SiO_2@$GdPO_4$:Tb@SiO_2 nanoparticles at different temperature ($\lambda_{ex} = 280$ nm). c(BSA) $= 1.0 \times 10^{-7}$ mol l^{-1}.

phosphate was protected from the perturbation of the surrounding environment, which contributed by SiO_2 shell. We have also studied the interaction between the as-prepared SiO_2@$GdPO_4$:Tb@SiO_2 nanoparticles and the BSA. The fluorescence spectra of BSA with increase of the SiO_2@$GdPO_4$:Tb@SiO_2 nanoparticles concentration at different temperature were measured as shown figure 6. It can be shown that the emission intensity of BSA decreases along with the increase of the nanoparticles concentration, which indicates that the intrinsic fluorescence of BSA can be quenched by adding SiO_2@$GdPO_4$:Tb@SiO_2 nanoparticles into BSA solution. Usually, the main fluorescence quenching mechanism of BSA is dynamics quenching or static quenching. The types of fluorescence quenching mechanisms can be distinguished by different dependence on temperature [26,27].

The fluorescence quenching intensities at 335 nm for the BSA plus SiO_2@$GdPO_4$:Tb@SiO_2 nanoparticles system at 293, 303 and 313 K were fitted by the below Stern–Volmer equation (3.1) [27,28]

$$\frac{F_0}{F} = 1 + K_q \tau_0 [Q] = 1 + K_{sv}[Q], \tag{3.1}$$

where F_0 and F are the emission intensities of BSA and BSA with nanoparticles, respectively; K_q is the maximum scatter collision quenching constant; τ_0 is the lifetime of the BSA, the value is approximately 10^{-8} s; K_{sv} is the Stern–Volmer quenching constant and [Q] is the concentration of SiO_2@$GdPO_4$:Tb@SiO_2 nanoparticles [29].

For this system, the K_{sv} could be obtained from the Stern–Volmer equation (3.1). The graph of F_0/F against [Q] at 293, 303 and 313 K were plotted (figure 7) and the corresponding data were summarized in table 1 for the quenching of BSA by SiO_2@$GdPO_4$:Tb@SiO_2 nanoparticles. The calculated values of K_{sv} were 1.0292×10^4 at 293 K ($R^2 = 0.975$), 1.0148×10^4 at 303 K ($R^2 = 0.981$) and 0.9189×10^4 l mol^{-1} at 313 K ($R^2 = 0.979$). The value of K_{sv} was decreased with rising temperature. It can be preliminarily estimated that the fluorescence quenching mechanism of BSA by SiO_2@$GdPO_4$:Tb@SiO_2 nanoparticles was initiated by the formation of a SiO_2@$GdPO_4$:Tb@SiO_2-protein complex. The fluorescence quenching mechanism of BSA by SiO_2@$GdPO_4$:Tb@SiO_2 nanoparticles was static quenching [30]. At

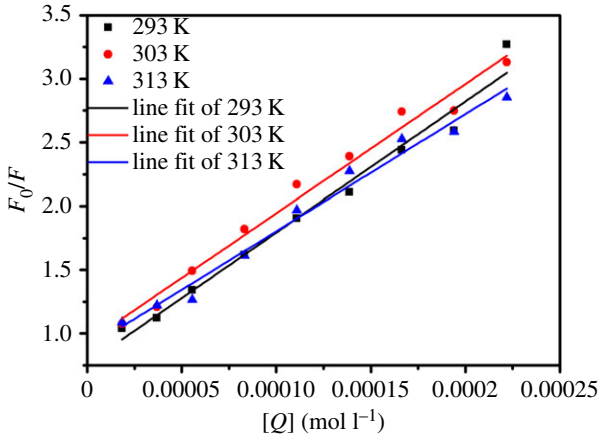

Figure 7. Stern–Volmer plots for the quenching of BSA by SiO_2@$GdPO_4$:Tb@SiO_2 at different temperature.

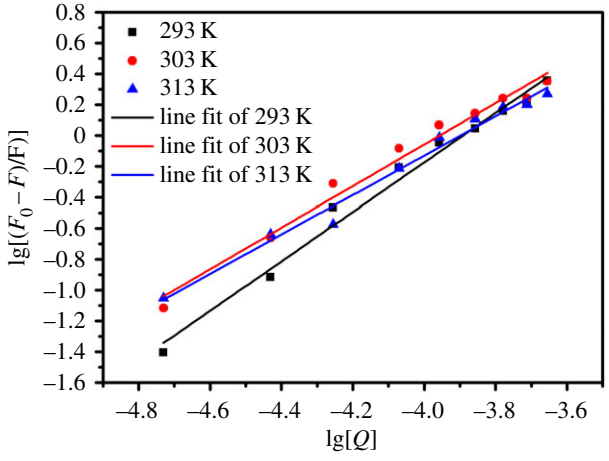

Figure 8. Relation curves of lg[$(F_0 - F)/F$)] and lg[Q] of SiO_2@$GdPO_4$:Tb@SiO_2.

Table 1. The parameters of Stern–Volmer plots for the fluorescence quenching of BSA by SiO_2@$GdPO_4$:Tb@SiO_2 at different temperature.

$T(K)$	Stern–Volmer linear equation	K_{sv} (l mol^{-1})	K_q($\times 10^{-8}$ l mol^{-1})	R^2
293	$F_0/F = 0.7637 + 1.0292[Q]$	1.0292×10^4	1.0292×10^4	0.975
303	$F_0/F = 0.9294 + 1.0148[Q]$	1.0148×10^4	1.0148×10^4	0.981
313	$F_0/F = 0.8842 + 0.9189[Q]$	0.9189×10^4	0.9189×10^4	0.979

the same time, we used the following Mineweaver–Burk curve equation to calculate the binding constants (K_a) and binding sites (n) for the BSA plus SiO_2@$GdPO_4$:Tb@SiO_2 nanoparticles:

$$\lg\left[\frac{F_0 - F}{F}\right] = \lg K_a + n \lg [Q], \tag{3.2}$$

where F, F_0 are the emission intensities of BSA and BSA with nanoparticles, and [Q] is the concentration of SiO_2@$GdPO_4$:Tb@SiO_2 nanoparticles. The relation curves of lg[$(F_0 - F)/F$)] and lg[Q] at 293, 303 and 313 K for SiO_2@$GdPO_4$:Tb@SiO_2 nanoparticles are shown in figure 8. The values of K_a and n at different temperature were measured from the intercept and slope values by the relation curves of lg[$(F_0 - F)/F$)] and lg[Q] (listed in table 2). According to table 2, K_a = 1.682×10^6 (293 K), 2.082×10^5 (303 K) and 9.313×10^4 l mol^{-1} (313 K) and n = 1.6002 (293 K), 1.3443 (303 K) and 1.2748 (313 K) for BSA-SiO_2@$GdPO_4$:Tb@SiO_2 nanoparticles system, respectively. It could be seen that the binding constants were

Table 2. Binding constants (K_a) and binding sites (n) of SiO_2@$GdPO_4$:Tb@SiO_2 nanoparticles with BSA at different temperature.

$T(K)$	equation	K_a (l mol^{-1})	n	R^2
293	$\lg[(F_0 - F)/F)] = 6.2264 + 1.6002\lg[Q]$	1.682×10^6	1.6002	0.984
303	$\lg[(F_0 - F)/F)] = 5.3185 + 1.3443\lg[Q]$	2.082×10^5	1.3443	0.979
313	$\lg[(F_0 - F)/F)] = 4.9691 + 1.2748\lg[Q]$	9.313×10^4	1.2748	0.982

decreased with rising the temperature, which indicates that the binding ability of BSA and SiO_2@$GdPO_4$:Tb@SiO_2 nanoparticles decreased.

4. Conclusion

The core-shell-shell structured SiO_2@$GdPO_4$:Tb@SiO_2 nanoparticles with uniform coating layer have been successfully synthesized at room temperature. The possible growth mechanism of SiO_2@$GdPO_4$:Tb@SiO_2 nanoparticles was proposed. The SiO_2@$GdPO_4$:Tb@SiO_2 nanoparticles have strong green luminescence. Interestingly, the emission intensity and the absolute quantum yield of $GdPO_4$:Tb nanoparticles were improved by the SiO_2 shell. The absolute quantum yield of SiO_2@$GdPO_4$:Tb@SiO_2 is about 10 times higher than that of $GdPO_4$:Tb nanoparticles. The interaction between the core-shell-shell structured nanoparticles and BSA was investigated through the fluorescence spectroscopy. The quenching mechanism of the fluorescence of BSA by SiO_2@$GdPO_4$:Tb@SiO_2 nanoparticles can be attributed to the static quenching.

Data accessibility. Our data are deposited at the Dryad Digital Repository: https://doi.org/10.5061/dryad.ttdz08ktf [31].

Authors' contributions. J.B. designed research; H.B., X.G and M.W. performed the experimental work. H.B. wrote the manuscript. H.B., Y.Y., J.B., A.W., Y.Q., X.G., M.W., W.L., Y.L., X.Z., contributed to the scientific discussion of the results. All authors gave final approval for publication.

Competing interests. The authors declare no competing interests.

Funding. This work was supported by the National Natural Science Foundations of China (21766021) and the Scientific Research Project of Colleges and Universities in Inner Mongolia Autonomous region (NJZZ19002). The project was also funded by the major basic research and open project of the Inner Mongolia Autonomous Region (30500-515330303).

Acknowledgements. All the people who contributed to the study are listed as co-authors.

References

1. Suresh C, Nagabhushana H, Basavaraj RB, Darshan GP, Kavyashree D, Daruka Prasad B, Sharma SC, Vanithamani R. 2018 SiO_2@LaOF:Eu^{3+} core-shell functional nanomaterials for sensitive visualization of latent fingerprints and WLED applications. *J. Colloid Interface Sci.* **518**, 200–215. (doi:10.1016/j.jcis.2018.01.093)
2. Rao RP, Devine DJ. 2000 RE-activated lanthanide phosphate phosphors for PDP applications. *J. Lumin.* **87–89**, 1260–1263. (doi:10.1016/S0022-2313(99)00551-7)
3. Lv RC, Yang GX, Gai SL, Dai YL, He F, Yang PP. 2014 Multifunctional $LaPO_4$:Ce/Tb@Au mesoporous microspheres: synthesis, luminescence and controllable light triggered drug release. *RSC Adv.* **4**, 63 425–63 435. (doi:10.1039/c4ra12942c)
4. Kuang XY, Liu H, Hu WY, Shao YZ. 2014 Hydrothermal synthesis of core-shell structured $TbPO_4$:Ce^{3+}@$TbPO_4$:Gd^{3+} nanocomposites for magnetic resonance and optical imaging. *Dalton Trans.* **43**, 12 321–12 328. (doi:10.1039/c4dt00249k)
5. Meenambal R, Poojar P, Geethanath S, Anitha TS, Kannan S. 2019 Lanthanide phosphate ($LnPO_4$) rods as bio-probes: a systematic investigation on structural, optical, magnetic, and biological characteristics. *J. Biomed. Mater. Res.* **107**, 1372–1383. (doi:10.1002/jbm.b.34229)
6. Meiser F, Cortez C, Caruso F. 2004 Biofunctionalization of fluorescent rare-earth doped lanthanum phosphate colloidal nanoparticles. *Angew. Chem. Int. Ed.* **43**, 5954–5957. (doi:10.1002/anie.200460856)
7. Lehmann O, Meyssamy H, Kompe K, Schnablegger H, Haase M. 2003 Synthesis, growth, and Er^{3+} luminescence of lanthanide phosphate nanoparticles. *J. Phys. Chem. B.* **107**, 7449–7453. (doi:10.1021/jp030012h)
8. Ren WL *et al.* 2012 Lanthanide ion-doped $GdPO_4$ nanorods with dual-modal bio-optical and magnetic resonance imaging properties. *Nanoscale* **4**, 3754–3760. (doi:10.1039/c2nr30683b)
9. Yin WY *et al.* 2012 Lanthanide-doped $GdVO_4$ upconversion nanophosphors with tunable emissions and their applications for biomedical imaging. *J. Mater. Chem.* **22**, 6974–6981. (doi:10.1039/c2jm16152d)
10. Rodriguez-Liviano S, Becerro AI, Alcantara D, Grazu V, de la Fuente JM, Ocana M. 2013 Synthesis and properties of multifunctional tetragonal Eu:$GdPO_4$ nanocubes for optical and magnetic sesonance imaging applications. *Inorg. Chem.* **52**, 647–654. (doi:10.1021/ic3016996)
11. Kumar V, Singh S, Kotnala RK, Chawla S. 2014 $GdPO_4$:Eu^{3+} nanoparticles with intense orange red emission suitable for solar spectrum conversion and their multifunctionality. *J. Lumin.* **146**, 486–491. (doi:10.1016/j.jlumin.2013.10.040)
12. Wu SS, Yin JC, Qu HB, Li AM, Liu LZ, Shao YZ. 2019 Photoluminescence properties of gadolinium phosphate nanoprisms doped with lanthanide ions for multicolor live cell imaging. *J. Mater. Sci. Mater. Electron* **30**, 11 336–11 345. (doi:10.1007/s10854-019-01481-z)
13. Ansari AA. 2017 Role of surface modification on physicochemical properties of luminescent YPO_4:

Tb nanorods. *Colloids Surf. A.* **529**, 286–291. (doi:10.1016/j.colsurfa.2017.05.028)

14. Zhang XY, Guo Z, Zhang X, Gong LJ, Dong XH, Fu YY, Wang Q, Gu ZJ. 2019 Mass production of poly (ethylene glycol) monooleate-modifed core-shell structured upconversion nanoparticles for bio-imaging and photodynamic therapy. *Sci. Rep.* **9**, 5212. (doi:10.1038/s41598-019-41482-w)
15. Yi GS, Chow GM. 2007 Water-soluble $NaYF_4$:Yb, Er(Tm)/$NaYF_4$/polymer core/shell/shell nanoparticles with significant enhancement of upconversion fluorescence. *Chem. Mater.* **19**, 341–343. (doi:10.1021/cm062447y)
16. Xu YL, Wang R, Zheng YX, Zhang LH, Jiao TF, Peng QM, Liu ZF. 2020 Facile preparation of self-assembled Ni/Co phosphates composite spheres with highly efficient HER electrocatalytic performances. *Appl. Surf. Sci.* **509**, 145383. (doi:10.1016/j.apsusc.2020.145383)
17. Zhao JX, Yin JJ, Zhong JL, Jiao TF, Bai ZH, Wang SF, Zhang LX, Peng QM. 2020 Facile preparation of a self-assembled Artemia cyst shell–TiO_2–MoS_2 porous composite structure with highly efficient catalytic reduction of nitro compounds for wastewater treatment. *Nanotechnology* **31**, 085603. (doi:10.1088/1361-6528/ab53c1)
18. Atabaev TS, Jin OS, Lee JH, Han DW, Vu HHT, Hwang YH, Kim HK. 2012 Facile synthesis of bifunctional silica-coated core–shell Y_2O_3:Eu^{3+}, Co^{2+} composite particles for biomedical applications. *RSC. Adv.* **2**, 9495–9501. (doi:10.1039/c2ra21332j)
19. Xu ZH, Gao Y, Huang SS, Ma PA, Lin J, Fang JY. A. 2011 Luminescent and mesoporous core-shell structured Gd_2O_3: Eu^{3+}@nSiO_2@mSiO_2 nanocomposite as a drug carrier. *Dalton Trans.* **40**, 4846–4854. (doi:10.1039/c1dt10162e)
20. Yang KS, Wu AP, Zhao X, Yan Y, Guo XY, Bian YL, Bao JR, Li WX, Zhu XW. 2017 Controlled synthesis of $EuPO_4$ nano/microstructures and core-shell SiO_2@$EuPO_4$ nanostructures with improved photoluminescence. *RSC Adv.* **7**, 52 238–52 244. (doi:10.1039/c7ra10556h)
21. Yang KS *et al.* 2018 Synthesis and photoluminescence properties of novel core-shell-shell SiO_2@$CePO_4$:Tb@SiO_2 submicro-spheres. *CrystEngComm* **20**, 6351–6357. (doi:10.1039/c8ce01189c)
22. Chen S, Osaka A, Hayakawa S, Tsuru K, Fujii E, Kawabata K. 2008 Microstructure evolution in Stober-type silica nanoparticles and their in vitro apatite deposition. *J. Sol. Gel Sci. Technol.* **48**, 322–335. (doi:10.1007/s10971-008-1823-z)
23. Wong KL, Law GL, Murphy MB, Tanner PA, Wong WT, Lam KS, Lam HW. 2008 Functionalized europium nanorods for in vitro imaging. *Inorg. Chem.* **47**, 5190–5196. (doi:10.1021/ic8000416)
24. Stöber W, Fink A, Bohn E. 1968 Controlled growth of monodisperse silica spheres in the micron size range. *J. Colloid Interface Sci.* **26**, 62–69. (doi:10.1016/0021-9797(68)90272-5)
25. Guo XD, Zhu GS, Fang QR, Xue M, Tian G, Sun JY, Li XT, Qiu SL. 2005 Synthesis, structure and luminescent properties of rare earth coordination polymers constructed from paddle-wheel building blocks. *Inorg. Chem.* **44**, 3850–3855. (doi:10.1021/ic0500457)
26. Ding F, Zhao GY, Chen SC, Liu F, Sun Y, Zhang L. 2009 Chloramphenicol binding to human serum albumin: determination of binding constants and binding sites by steady-state fluorescence. *J. Mol. Struct.* **929**, 159–166. (doi:10.1016/j.molstruc.2009.04.018)
27. Guo XJ, Yao J, Liu XH, Wang HY, Zhang LZ, Xu LP, Hao AJ. 2018 $LaPO_4$:Eu fluorescent nanorods, synthesis, characterization and spectroscopic studies on interaction with human serum albumin. *Spectrochim. Acta, Part A* **198**, 248–256. (doi:10.1016/j.saa.2018.02.066)
28. Kong DY, Qin C, Fan P, Li B, Wang J. 2015 Spectroscopic studies on interaction of BSA and Eu(III) complexes with H_5ph-dtpa and H_5dtpa ligands. *Spectrochim. Acta, Part A* **140**, 372–381. (doi:10.1016/j.saa.2015.01.004)
29. Karami K, Rahimi M, Zakariazadeh M, Buyukgungor O, Momtazi-Borojeni AA, Esmaeili SA. 2019 A novel silver (I) complex of a-keto phosphorus ylide: synthesis, characterization, crystal structure, biomolecular interaction studies, molecular docking and in vitro cytotoxic evaluation. *J. Mol. Struct.* **1177**, 430–443. (doi:10.1016/j.molstruc.2018.09.063)
30. Tunc S, Duman O, Soylu I, Bozoglan BK. 2014 Study on the bindings of dichlorprop and diquat dibromide herbicides to human serum albumin by spectroscopic methods. *J. Hazard. Mater.* **273**, 36–43. (doi:10.1016/j.jhazmat.2014.03.022)
31. Bai H *et al.* 2020 Data from: High-efficient fabrication of core-shell-shell structured SiO_2@$GdPO_4$:Tb@SiO_2 nanoparticles with improved luminescence. Dryad Digital Repository. (doi:10.5061/dryad.ttdz08ktf)